

Signal-SGN: A Spiking Graph Convolutional Network for Skeleton Action Recognition via Learning Temporal-Frequency Dynamics

Naichuan Zheng, Yuchen Du, Hailun Xia, Dapeng Liu

Beijing Laboratory of Advanced Information Networks,

Beijing Key Laboratory of Network System Architecture and Convergence,

School of Information and Communication Engineering,

Beijing University of Posts and Telecommunications,

Beijing, China, 100876

{2022110134zhengnaichuan, duyuche, nxiahailun, ldp0621}@bupt.edu.cn

Abstract—For skeleton-based action recognition, Graph Convolutional Networks (GCNs) are effective models. Still, their reliance on floating-point computations leads to high energy consumption, limiting their applicability in battery-powered devices. While energy-efficient, Spiking Neural Networks (SNNs) struggle to model skeleton dynamics, leading to suboptimal solutions. We propose Signal-SGN (Spiking Graph Convolutional Network), which utilizes the temporal dimension of skeleton sequences as the spike time steps and represents features as multi-dimensional discrete stochastic signals for temporal-frequency domain feature extraction. It combines the 1D Spiking Graph Convolution (1D-SGC) module and the Frequency Spiking Convolution (FSC) module to extract features from the skeleton represented as spiking form. Additionally, the Multi-Scale Wavelet Transform Feature Fusion (MWTF) module is proposed to extract dynamic spiking features and capture frequency-specific characteristics, enhancing classification performance. Experiments across three large-scale datasets reveal Signal-SGN exceeding state-of-the-art SNN-based methods in accuracy and computational efficiency while attaining comparable performance with GCN methods and significantly reducing theoretical energy consumption.

Index Terms—Skeleton-based Action Recognition, Spiking Neural Networks, Frequency Domain Transform

I. INTRODUCTION

Skeleton-based action recognition, as a critical subfield of human action recognition, has made significant strides in recent years. Leveraging sparse representations obtained from pose estimation and sensor-based data, it enables effective classification of human actions [1]. Numerous methods have been proposed for this task, including CNNs [2], LSTMs [3], Transformers [4], and Graph Convolutional Networks (GCNs) [5]. Among them, ST-GCN is a pioneering method that laid the foundation for GCN-based approaches [6]. Several methods, such as 2s-AGCN [7] and Dynamic GCN [8], have been proposed subsequently, further improving accuracy in action recognition. Lightweight models like Shift-GCN [5] and CTR-GCN [9] have further enhanced accuracy while reducing computational costs. However, these methods are all based on artificial neural networks (ANNs), which rely on floating-point

operations (FLOPs), leading to significant energy consumption that limits their practicality in energy-constrained applications.

Spiking Neural Networks (SNNs), regarded as third-generation neural networks, utilize spike-form features encoded as 0s and 1s to mimic neural dynamics. Unlike ANNs, SNNs process information in an event-driven manner, enabling significantly lower energy consumption while maintaining efficient computation [10]. Various SNN models have been proposed, leveraging their energy efficiency, and have been applied to a wide range of tasks, including image classification and point cloud estimation [11]–[15]. Among these, Spiking Graph Networks (SGNs) combine graph convolution with SNNs, achieving remarkable energy savings. For instance, SGNs reduce energy consumption by nearly 99% compared to vanilla GCNs [16]. Specifically, SGN has been utilized for skeleton action recognition, cutting energy consumption to less than 5% of GCNs while maintaining comparable accuracy [17]. Despite its advantages, [17] treats dynamic skeleton data as static image data, artificially extending it along the spike time step dimension. This approach neglects the time-sensitive computational capabilities of SNNs, failing to effectively capture the inherent temporal dynamics of skeleton data. As a result, it increases computational complexity, hampers performance, and poses significant challenges for efficient training on standard deep-learning hardware. Furthermore, SGNs, like other SNN-based models [13]–[15], perform a simplistic Global Average Pooling (GAP) over the spike time step dimension in the task head, failing to thoroughly analyze the discrete and aperiodic nature of spike-form features. This oversimplification limits the model’s ability to capture temporal patterns, reducing its task performance.

To overcome these challenges, we propose Signal-SGN for skeleton action recognition, utilizing the temporal dimension of skeleton sequences as the spiking time step and representing skeleton data as spiking-form features with multi-dimensional discrete stochastic properties. The architecture comprises two primary modules: a one-dimensional Spiking Graph Convolution (1D-SGC) module and a Frequency Spik-

ing Convolution (FSC) module. The 1D-SGC extracts feature from single-frame skeleton graphs within temporal sequences and represents them as the spiking-form. Meanwhile, the FSC utilizes the Fast Fourier Transform (FFT) to transform the spiking-form features of each frame into frequency-domain and leverages complex spiking convolution for advanced feature extraction. Through successive 1D-SGC-FSC layers, the features remain discrete and aperiodic. We formulate a Multi-Scale Wavelet Transform Feature Fusion (MWTF) module to address the limitations of simple GAP, which fails to effectively capture the temporal dynamics and frequency-specific characteristics of spiking-form features. The module exploits discrete wavelet transform (DWT) to decompose features into distinct frequency components and integrates a spiking cross-attention mechanism for robust feature fusion. The proposed module significantly improves classification performance. Our main contributions can be summarized as follows:

- We propose a novel Signal-SGN network comprising multi-layer 1D-SGC-FSC that captures temporal-frequency domain spatial features of single-frame skeleton graphs and leverages the time-sensitive computational properties of SNNs to effectively model sequence-level temporal dynamics.
- We propose the MWTF module, which achieves multi-scale frequency-domain decomposition and interaction between frequency-specific features to extract dynamic spiking features, capture frequency-specific characteristics, and improve classification performance.
- Extensive experiments across three large-scale demonstrate that Signal-SGN surpasses State-of-the-Art (SOTA) SNN methods in terms of computational costs, and accuracy while achieving results comparable to GCN-based methods with significantly lower energy consumption.

II. RELATED WORK

A. Skeleton-Based Action Recognition.

Deep learning methods have played a significant role in skeleton-based action recognition. Early approaches in this field achieved significant success using CNNs [2] and RNNs [3]. Subsequent research has primarily focused on using Transformers [4] and GCNs [5]–[7], [9], [18]. These numerous GCN-based methods typically involve nearly multi-layer stacks of Graph Convolutional Networks and Temporal Convolutional Networks. However, GCN-based networks are intrinsically tied to ANN architectures, which rely on floating-point computations. Such reliance leads to substantial energy consumption and fundamentally misaligns with practical requirements for energy-efficient solutions.

B. Spiking Neural Networks.

SNNs, inspired by biological neural networks, offer an energy-efficient alternative to traditional neural networks [10]. They can be implemented through two primary approaches: ANN-to-SNN conversion [19] and direct training using algorithms like STDP [20] or surrogate gradients [21]. The fundamental units, such as Leaky Integrate-and-Fire (LIF) neurons,

are notable for their simplicity and biological plausibility [22]. The differential equation describes the dynamics of the LIF neuron:

$$\tau_m \frac{dV(t)}{dt} = -V(t) + R \cdot I(t), \quad (1)$$

where $V(t)$ is the membrane potential, τ_m is the time constant indicating potential decay, R is the membrane resistance, and $I(t)$ is the input current. When $V(t)$ reaches the threshold V_{th} , the neuron fires a spike and resets to V_{reset} . The LIF neuron model accurately replicates the spiking dynamics characteristic of neurons within SNNs.

Inspired by ANN architectures, corresponding SNN models have been proposed and applied to tasks such as image classification, event-driven processing, and EEG analysis [23]–[25]. Among these, various spiking-based Transformers have played significant roles [13]–[15]. Meanwhile, [17] introduces Spiking Graph Networks (SGNs) for skeleton-based action recognition for the first time, achieving promising results. However, [17] treats the skeleton sequence data as static and artificially extends them along the spike time step dimension, which increases storage and computational demands. Additionally, SGNs fail to capture the discrete and non-periodic nature of spike-form features and rely on simple GAP to reduce the spike time step dimension before the classification head, limiting classification performance and accuracy.

C. Frequency Domain Analysis.

In neural network design, frequency domain analysis is crucial for improving performance and robustness. The FFT and Wavelet Transform (WT) enhance feature extraction within CNNs for applications such as image compression [26]. FFT also plays an important role in sequential data analysis within RNNs, which is particularly beneficial for applications such as speech recognition [27]. GCNs integrate Fourier transforms (FT) to analyze graph signals [28]. Meanwhile, SNNs combined with WT enable effective spatial-frequency domain learning, achieving energy efficiency and high performance [29]. In the context of SNNs, skeleton sequences are represented as spiking-form feature, resembling discrete multi-dimensional stochastic signals. Exploring their frequency domain characteristics has significant potential for the analysis of skeleton action recognition within SNNs. However, research in the area is currently insufficient.

III. METHOD

This section presents the overall architecture of Signal-SGN, provided in Figure 1. It begins with a description of the backbone network, including the 1D-SGC module and the FSC module, which constitute the core components of the model. Following this, the MWTF module is explained, emphasizing its role for enhancing performance.

A. The Backbone of Signal-SGN

As illustrated in Figure 1, Signal-SGN processes three-dimensional skeleton data $X \in \mathbb{R}^{C \times T \times V}$, where C represents spatial coordinates (x, y, z), T denotes the number of frames and spike time steps, and V is the number of joints per

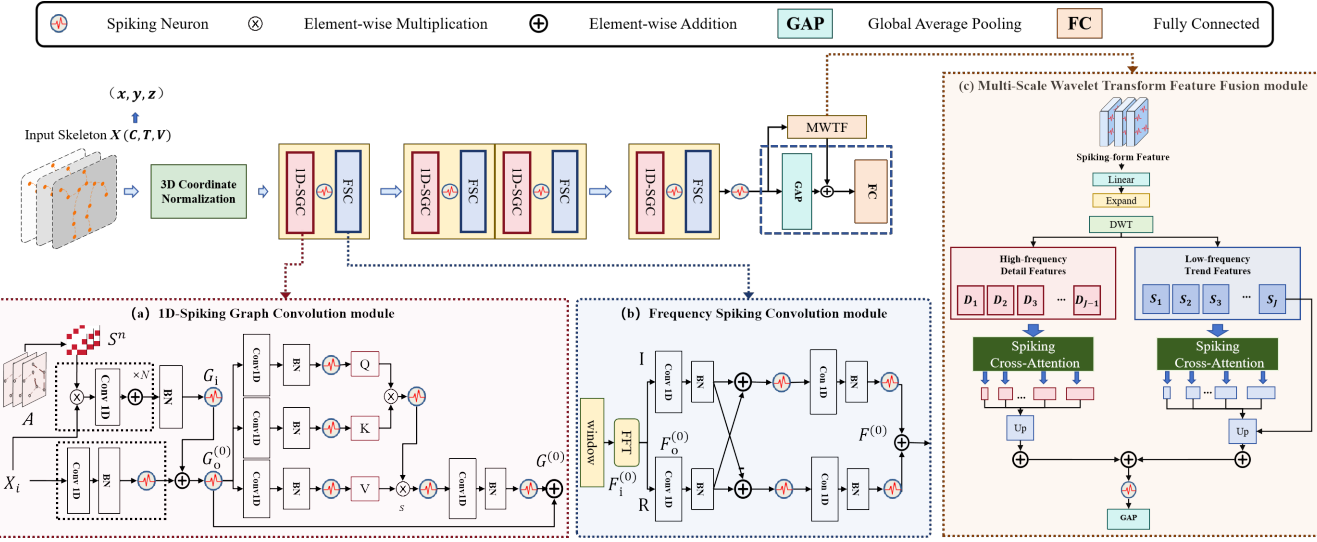


Fig. 1. The overview of the proposed Signal-SGN method.

frame. The spatial coordinates, which contain both positive and negative values, pose challenges to SNNs due to rate coding and binarization, leading to information loss. To address this, the coordinates are normalized to $[0, 1]$ using the formula $a' = (a - a_{\min}) / (a_{\max} - a_{\min})$, where $a \in \{x, y, z\}$. After normalization, the skeleton data is transformed into $X_i \in \mathbb{R}^{T \times C' \times V}$, where C' corresponds to the normalized three-dimensional coordinates.

In the 1D-SGC module, inspired by GCN, we integrate topological information by normalizing adjacency-based weights to aggregate attributes from neighboring nodes, as shown in Figure 1(a). The skeleton can be represented as a graph $\mathcal{G}(V, E)$, where the joints form a set of vertices V and the bones represent the edges E . This structure can be expressed as an adjacency matrix $A \in \mathbb{R}^{V \times V}$, where $A_{i,j} = 1$ if joints i and j are physically connected, and $A_{i,j} = 0$ otherwise. To incorporate topological relationships into computations, the normalized adjacency matrix S is computed as follows:

$$S = \Delta^{-\frac{1}{2}} \tilde{A} \Delta^{-\frac{1}{2}}, \quad (2)$$

where $\tilde{A} = A + I$ is the adjacency matrix with added self-connections, and Δ is the degree matrix of \tilde{A} . This normalization ensures that the influence of each node is appropriately scaled based on its connectivity, facilitating the effective integration of topological information into the model. Subsequently, we apply one-dimensional convolution (Conv1d) and one-dimensional Batch Normalization(BN) along the C' dimension to extract features for each skeleton node within each spike time step, effectively aggregating features across the skeleton joints dimension.

$$G_i = \text{BN} \left[\sum_{n=0}^N \text{Conv1d} (X_i * S^n) \right], \quad (3)$$

in which S^n represents a set of matrices decomposed from S , N refers to the number of different relational matrices in the decomposition, and $*$ denotes matrix multiplication. The resulting output $G_i \in \mathbb{R}^{T \times D \times V}$, where D represents the hidden channel dimension.

To leverage the temporal dynamic characteristics of SNNs, we map the inherent temporal dimension of the features to the spike time steps of the SNNs and input the features into spiking neurons (SN). The Algorithm 1 outlines the detailed process provided in the Appendix V-B1. For compactness, we define the operation $SN[\text{BN}(\text{Conv1d}(\cdot))]$ as $\Phi(\cdot)$. The updated formula becomes:

$$G_o^{(0)} = SN(G_i) + \Phi(X_i). \quad (4)$$

Building upon the approach proposed in [13], we integrate the spike self-attention (SSA) mechanism after the graph convolution operation to enhance feature representation. The formula is as follows:

$$Q^{(0)} = \Phi_Q(G_o^{(0)}), K^{(0)} = \Phi_K(G_o^{(0)}), V^{(0)} = \Phi_V(G_o^{(0)}), \quad (5)$$

$$G^{(0)} = G_o^{(0)} + \Phi \left(Q^{(0)} K^{(0)T} V^{(0)} * s \right), \quad (6)$$

where s is the scaling factor to control the large value of the matrix multiplication result.

Following the 1D-SGC module, the features are retransformed by SN into spiking-form feature—discrete, aperiodic signal sequences encoded as binary values (0s and 1s). To further extract meaningful frequency-domain feature, we propose the FSC module, as shown in Figure 1(b). This module first leverages a learnable window function applied along the joint dimension V to mitigate spectral leakage, enhancing the precision of frequency-domain analysis and improving feature extraction robustness, defined as:

$$w_V(v) = \alpha - (1 - \alpha) \cdot \cos \left(\frac{2\pi v}{V-1} \right), \quad 0 \leq v \leq V-1. \quad (7)$$

where v is the joint index and α is a learnable parameter controlling the window shape. The learnability of α allows the module to adapt the window function to specific characteristics. The windowed features are then processed as:

$$F_i^{(0)} = w_V(v) \cdot SN(G^{(0)}) \in \mathbb{R}^{T \times D \times V}. \quad (8)$$

We apply FFT along the V dimension to transform the features from the temporal domain to the frequency domain:

$$F_o^{(0)} = \sum_{v=0}^{V-1} F_i^{(0)} e^{-j2\pi \frac{mv}{V}} = F_R^{(0)} + jF_I^{(0)}, \quad (9)$$

where $F_o^{(0)} \in \mathbb{C}^{T \times D \times M}$, and $m \in [0, M-1]$ represents the frequency index, determining the frequency components extracted along the V dimension. To process the complex-valued FFT outputs, we propose a spiking complex convolution module that preserves and utilizes amplitude and phase information, enhancing the network's ability to capture detailed frequency-domain features:

$$F_{o,R}^{(0)} = BN[\text{Conv1d}(F_R^{(0)})], F_{o,I}^{(0)} = BN[\text{Conv1d}(F_I^{(0)})], \quad (10)$$

$$F_{o,k}^{(0)} = SN\left(F_{o,R}^{(0)} \pm_k F_{o,I}^{(0)}\right), \quad k \in \{1, 2\}. \quad (11)$$

where \pm_k represents addition (+) when $k=1$, and subtraction (-) when $k=2$. The fused output is then computed as:

$$F^{(0)} = \Phi\left(F_{o,1}^{(0)}\right) + \Phi\left(F_{o,2}^{(0)}\right). \quad (12)$$

The output $F^{(0)}$ represents the extracted frequency-domain features, serving as an essential input for the subsequent layers of the network.

A complete 1D-SGC-FSC process can then be expressed as:

$$X^{(l)} = F^{(l)} + G^{(l)} + \text{res}\left(G^{(l-1)}\right), \quad (13)$$

where, $X^{(l)}$ denotes the output of the l -th layer, combining the frequency-domain features $F^{(l)}$, temporal-domain features $G^{(l)}$, and a residual connection from the previous layer $\text{res}\left(G^{(l-1)}\right)$.

B. Multi-Scale Wavelet Transform Feature Fusion module

We formulate the MWTF module to capture the temporal dynamics and frequency-specific characteristics of spiking-form features, with its outputs fused with backbone outputs to enhance classification performance, as illustrated in Figure 1(c).

We first construct filters $\Lambda_0, \Lambda_1, \Gamma_0$, and Γ_1 based on Legendre polynomials $P_k(x)$ (details are provided in Appendix V-A) to decompose spiking-form features. The parameter k specifies the number of frequency coefficients extracted, influencing the spectral resolution. We apply a linear (LN) transformation to the spiking features from the final layer L of the backbone network to align the output tensor with the k coefficients, ensuring compatibility with the filters.

$$X_{\text{down}} = LN\left(SN\left(X^{(L)}\right)\right) \in \mathbb{R}^{T \times k \times V}. \quad (14)$$

To ensure compatibility with the wavelet transform, we verify whether the temporal dimension T is a power of two. If not, X_{down} is padded to the nearest power of two:

$$X_{\text{extra}} = X_{\text{down}}[0 : (2^{\lceil \log_2(T) \rceil} - T), :, :], \quad (15)$$

$$X_{\text{extended}} = \text{concat}(X_{\text{down}}, X_{\text{extra}}, \text{axis} = 1), \quad (16)$$

The extended spike-form feature X_{extended} is decomposed by the filter matrices $\Lambda_0, \Lambda_1, \Gamma_0$, and Γ_1 into detail coefficients D_j , capturing high-frequency detailed features, and scaling coefficients S_j , retaining low-frequency trend features. The Algorithm 2 in Appendix V-B2 details the complete process.

To enhance the interaction between detail coefficients D_j and scaling coefficients S_j across decomposition levels j , we redefine the spiking cross-attention operation as:

$$D_j^{\text{out}} = (\Phi_Q(D_j) \cdot \Phi_K(D_j)^T) \Phi_V(S_j) * s, \quad (17)$$

$$S_j^{\text{out}} = (\Phi_Q(S_j) \cdot \Phi_K(S_j)^T) \Phi_V(D_j) * s, \quad (18)$$

where the temporal resolution is halved at each level. At the final level J , the scaling coefficient S_J bypasses cross-attention and is directly upsampled to match the temporal resolution $T/2$:

$$\hat{S}_J = \text{Upsample}(S_J, T/2). \quad (19)$$

All previous levels' outputs $\{D_j^{\text{out}}, S_j^{\text{out}}\}_{j=0}^{J-1}$ are similarly upsampled, and the aggregated feature map is computed as:

$$X_{\text{MLO}} = \text{GAP}\left(\Phi\left(\sum_{j=0}^{J-1} \hat{D}_j + \sum_{j=0}^J \hat{S}_j\right)\right). \quad (20)$$

The final feature map X_{MLO} integrates dynamic spiking features and spectral characteristics, which are fused with the output $X^{(L)}$ from the last backbone layer undergoing SN and GAP . Then the fused feature proceed to a fully connected (FC) layer for classification:

$$\hat{y} = \text{FC}\left(\text{GAP}\left(SN\left(X^{(L)}\right)\right) + \beta X_{\text{MLO}}\right), \quad (21)$$

where β is a learnable parameter. Finally, the cross-entropy loss is employed to optimize the classification task.

IV. EXPERIMENTS

We evaluate the Signal-SGN model on three skeleton-based action recognition datasets: NTU-RGB+D [30], NTU-RGB+D 120 [31], and NW-UCLA [32]. Detailed descriptions of the datasets, along with hyperparameter design, FLOPs, synaptic operations (SOPs), and theoretical energy consumption calculations, are provided in the Appendix V-C, V-D and V-E.

TABLE I

COMPARATIVE RESULTS ON NTU RGB+D AND NTU-RGB+D 120. WE EVALUATE OUR MODEL IN TERMS OF CLASSIFICATION ACCURACY (%). Xs AND Xv REPRESENT CROSS-SUBJECT AND CROSS-VIEW SPLITS.

Model (ANN/SNN)	Param. (M)	FLOPs (G)	SOPs (G)	Power (mJ)	Xs (60)	Xv (60)	Xs (120)	Xv (120)
Part-aware LSTM [33]	-	-	-	-	62.9	70.3	25.5	26.3
Spatio-Temporal LSTM [34]	-	-	-	-	61.7	75.50	55.7	57.9
ST-GCN [6]	3.10	3.48	-	16.01	81.5	88.3	70.7	73.2
2S-AGCN [7]	3.48	37.32	-	182.87	88.5	95.1	82.5	84.3
Shift-GCN [5]	-	10.00	-	46.0	90.7	96.5	85.3	86.6
MS-G3D [35]	3.19	48.88	-	239.51	91.5	96.2	86.9	88.4
CTR-GCN [9]	1.46	7.88	-	36.25	92.4	96.8	88.9	90.6
Spikformer [13] ^{ICLR 2023}	4.78	24.07	1.69	2.17	73.9	80.1	61.7	63.7
Spike-driven Transformer [14] ^{NIPS 2023}	4.77	23.50	1.57	1.93	73.4	80.6	62.3	64.1
Spike-driven Transformer V2 [15] ^{ICLR 2024}	11.47	38.28	2.59	2.91	77.4	83.6	64.3	65.9
Spiking Wavelet Transformer [29] ^{ECCV 2025}	3.24	19.3	1.48	2.01	74.7	81.2	63.5	64.7
MK-SGN [17]	2.17	7.84	0.68	0.614	78.5	85.6	67.8	69.5
Signal-SGN (Joint)	1.74	1.62	0.314	0.372	80.5	87.7	69.2	72.1
Signal-SGN (Bone+Joint)	1.74	3.24	0.628	0.744	82.5	89.2	71.3	74.2
Signal-SGN (4 ensemble)	1.74	6.48	1.28	1.488	86.1	93.1	75.3	77.9

The Param. represents the model size for the network itself. For ANN, the metrics such as FLOPs, power, and accuracy are reported and calculated based on the maximum ensemble of modalities as specified in the referenced paper.

TABLE II

COMPARATIVE RESULTS ON NW-UCLA. WE EVALUATE OUR MODEL IN TERMS OF CLASSIFICATION ACCURACY (%).

Model (ANN/SNN)	Param. (M)	FLOPs (G)	SOPs (G)	Power (mJ)	Acc (%)
Ensemble TS-LSTM [3]	-	-	-	-	89.2
DC-GCN+ADG [18]	2.48	3.6	-	16.56	95.3
CTR-GCN [9]	1.46	2.32	-	10.67	96.5
Spikformer [13] ^{ICLR 2023}	4.78	8.55	0.513	0.673	85.4
Spike-driven Transformer [14] ^{NIPS 2023}	4.77	8.22	0.501	0.643	83.4
Spike-driven Transformer V2 [15] ^{ICLR 2024}	11.47	11.96	0.717	0.841	89.4
Spiking Wavelet Transformer [29] ^{NIPS 2023}	3.24	7.36	0.438	0.573	86.7
MK-SGN [17]	2.17	3.66	0.165	0.207	92.3
Signal-SGN (Joint)	1.74	0.67	0.161	0.147	92.7
Signal-SGN (Bone+Joint)	1.74	1.24	0.322	0.294	93.1
Signal-SGN (4 ensemble)	1.74	2.48	0.644	0.588	95.9

A. Comparison with the State-of-the-Art

Several SOTA methods have adopted multi-stream fusion strategies [5], [7], [9]. For a fair comparison, we implement the same four-stream fusion approach for our Signal-SGN, incorporating "joint", "bone," "joint motion", and "bone motion." We compare Signal-SGN with state-of-the-art methods across three datasets. To compare with SOTA SNN models [13]–[15], [29], we perform unimodal reproductions using the same hierarchical architecture as MK-SGN [17], demonstrating the superiority of our method. The parameters of our Signal-SGN model, including FLOPs, SOPs, energy consumption, and accuracy for both single-modal and multi-modal scenarios, are presented in Tables I and II. In the NTU-RGB+D dataset, we resize the skeleton sequences to 16 frames, our model outperforms SOTA SNN models in accuracy while significantly reducing FLOPs, SOPs, and theoretical energy consumption when using single-modality joint data. Furthermore, compared

to classical ANN models, our model achieves a higher accuracy than ST-GCN when integrating four modalities, which is quite rare for SNN. Our model also requires fewer FLOPs than the lightweight CTR-GCN and Shift-GCN models. In terms of theoretical energy consumption, our model reduces the energy usage to less than 5% compared to GCN-based methods, which is highly significant in practical applications.

In the NW-UCLA dataset, we also resize the skeleton sequences to 16 frames. Our model achieves an accuracy of 95.9%, which is only 0.6% lower than the classic CTR-GCN model while reducing theoretical energy consumption to 5.51% of CTR-GCN's. This further demonstrates the effectiveness and energy-saving capabilities of our model. Additionally, removing the extra spike time step dimension reduces FLOPs and improves memory efficiency, making the model more trainable on standard devices compared to the previous SGN model.

B. Ablation Studies

To evaluate the contributions of the primary components in Signal-SGN, we conducted ablation studies on the NTU-RGB+D (cross-subject) dataset using joint data, with all skeleton sequences resized to 16 frames. Table III summarizes classification performance for different main module configurations. Appendix V-F presents a detailed analysis. When only the 1D-SGC module is used, the model achieves an accuracy of 70.5%, demonstrating its ability to extract spiking-form graph features while maintaining low parameter count (1.03M) and computational costs (1.12G FLOPs/0.252G SOPs). Introducing FSC module significantly improves accuracy to 78.3%, highlighting the role of frequency-domain feature extraction in enhancing representations. The addition results in a moderate increase in parameter count to 1.65M and computational costs to 1.60G FLOPs/0.312G SOPs. Fi-

TABLE III
COMPARISON OF EXPERIMENTAL RESULTS UNDER DIFFERENT MODULE SETTINGS

Method	1D-SGC	FSC	MWTF	Param.	FLOPs/SOPs	Acc
				(M)	(G)	(%)
Ours	✓	-	-	1.03	1.12/0.252	70.5
	✓	✓	-	1.65	1.60/0.312	78.3
	✓	✓	✓	1.74	1.62/0.314	80.5

nally, incorporating the MWTF module further boosts accuracy to 80.5%. The improvement comes with a marginal parameter increase (1.74M) and computational costs (1.62G FLOPs/0.314G SOPs), demonstrating the MWTF module's effectiveness in capturing multi-scale frequency features and fusing temporal and spectral information. These results validate the complementary roles of the 1D-SGC, FSC, and MWTF modules. The 1D-SGC module focuses on temporal-domain graph features, while the FSC module captures frequency-domain information. The MWTF module further enhances the model by integrating multi-scale frequency features, establishing Signal-SGN as an efficient framework for skeleton-based action recognition.

V. CONCLUSION

We propose a novel Signal-SGN, a SNN-based framework designed to learn dynamic features in both the temporal and frequency domains for skeleton-based action recognition. The model comprises multiple stacked 1D-SGC-FSC layers, which utilize SGN to extract temporal-domain features from skeletons converted into spike forms and employ FFT and spiking complex convolution to extract frequency-domain feature. Additionally, the MWTF module, decomposes the spiking-form feature into distinct frequency components for robust feature fusion, enhancing classification performance, significantly. The final model surpasses SOTA SNNs in various aspects and achieves accuracy comparable to traditional ANN models while maintaining extremely low energy consumption, demonstrating its effectiveness and efficiency in skeleton-based action recognition.

REFERENCES

- [1] B. Ren, M. Liu, R. Ding, and et al, "A survey on 3d skeleton-based action recognition using learning method," *Cyborg and Bionic Systems*, vol. 5, pp. 0100, 2024.
- [2] Y. Du, Y. Fu, and L. Wang, "Skeleton based action recognition with convolutional neural network," in *2015 3rd IAPR Asian conference on pattern recognition (ACPR)*. IEEE, 2015, pp. 579–583.
- [3] Z. Gao, P. Wang, P. Lv, and et al, "Focal and global spatial-temporal transformer for skeleton-based action recognition," in *Proceedings of the Asian Conference on Computer Vision*, 2022, pp. 382–398.
- [4] C. Plizzari, M. Cannici, and M. Matteucci, "Skeleton-based action recognition via spatial and temporal transformer networks," *Computer Vision and Image Understanding*, vol. 208, pp. 103219, 2021.
- [5] K. Cheng, Y. Zhang, X. He, and et al., "Skeleton-based action recognition with shift graph convolutional network," in *Proceedings of the IEEE/CVF conference on computer vision and pattern recognition*, 2020, pp. 183–192.
- [6] Lin D. Yan S., Xiong Y., "Spatial temporal graph convolutional networks for skeleton-based action recognition," in *Proceedings of the AAAI Conference on Artificial Intelligence*, 2018, vol. 32.
- [7] L. Shi, Y. Zhang, J. Cheng, and et al, "Two-stream adaptive graph convolutional networks for skeleton-based action recognition," in *Proceedings of the IEEE/CVF conference on computer vision and pattern recognition*, 2019, pp. 12026–12035.
- [8] F. Ye, S. Pu, Q. Zhong, and et al, "Dynamic gen: Context-enriched topology learning for skeleton-based action recognition," in *Proceedings of the 28th ACM international conference on multimedia*, 2020, pp. 55–63.
- [9] Y. Chen, Z. Zhang, C. Yuan, and et al, "Channel-wise topology refinement graph convolution for skeleton-based action recognition," in *Proceedings of the IEEE/CVF international conference on computer vision*, 2021, pp. 13359–13368.
- [10] Adeli H. Ghosh-Dastidar S., "Spiking neural networks," *International journal of neural systems*, vol. 19, no. 04, pp. 295–308, 2009.
- [11] K. Yamazaki, V.-K. Vo-Ho, D. Bulsara, and et al, "Spiking neural networks and their applications: A review," *Brain Sciences*, vol. 12, no. 7, pp. 863, 2022.
- [12] A. Tavanaei, M. Ghodrati, S. R. Kheradpisheh, and et al, "Deep learning in spiking neural networks," *Neural networks*, vol. 111, pp. 47–63, 2019.
- [13] Z. Zhou, Y. Zhu, C. He, and et al, "Spikformer: When spiking neural network meets transformer," *arXiv preprint arXiv:2209.15425*, 2022.
- [14] M. Yao, J. Hu, Z. Zhou, and et al, "Spike-driven transformer," *Advances in neural information processing systems*, vol. 36, 2024.
- [15] M. Yao, J. Hu, T. Hu, and et al, "Spike-driven transformer v2: Meta spiking neural network architecture inspiring the design of next-generation neuromorphic chips," *arXiv preprint arXiv:2404.03663*, 2024.
- [16] Z. Zhu, J. Peng, J. Li, and et al, "Spiking graph convolutional networks," *arXiv preprint arXiv:2205.02767*, 2022.
- [17] N. Zheng, H. Xia, and Z. Liang, "Mk-sgn: A spiking graph convolutional network with multimodal fusion and knowledge distillation for skeleton-based action recognition," *arXiv preprint arXiv:2404.10210*, 2024.
- [18] K. Cheng, Y. Zhang, C. Cao, and et al, "Decoupling gen with drograph module for skeleton-based action recognition," in *Computer Vision-ECCV 2020: 16th European Conference, Glasgow, UK, August 23–28, 2020, Proceedings, Part XXIV 16*. Springer, 2020, pp. 536–553.
- [19] Nguyen-Dong Ho and Ik-Joon Chang, "Tcl: an ann-to-snn conversion with trainable clipping layers," in *2021 58th ACM/IEEE Design Automation Conference (DAC)*. IEEE, 2021, pp. 793–798.
- [20] N. Caporale and Y. Dan, "Spike timing-dependent plasticity: a hebbian learning rule," *Annu. Rev. Neurosci.*, vol. 31, no. 1, pp. 25–46, 2008.
- [21] Zenke F. Neftci E. O., Mostafa H., "Surrogate gradient learning in spiking neural networks: Bringing the power of gradient-based optimization to spiking neural networks," *IEEE Signal Processing Magazine*, vol. 36, no. 6, pp. 51–63, 2019.
- [22] C. Teeter, R. Iyer, V. Menon, and et al, "Generalized leaky integrate-and-fire models classify multiple neuron types," *Nature communications*, vol. 9, no. 1, pp. 709, 2018.
- [23] Khosla D. Cao Y., Chen Y., "Spiking deep convolutional neural networks for energy-efficient object recognition," *International Journal of Computer Vision*, vol. 113, pp. 54–66, 2015.
- [24] G. Pedretti, P. Mannocci, S. Hashemkhani, and et al, "A spiking recurrent neural network with phase-change memory neurons and synapses for the accelerated solution of constraint satisfaction problems," *IEEE Journal on Exploratory Solid-State Computational Devices and Circuits*, vol. 6, no. 1, pp. 89–97, 2020.
- [25] S. Cai, R. Zhang, M. Zhang, and et al, "Eeg-based auditory attention detection with spiking graph convolutional network," *IEEE Transactions on Cognitive and Developmental Systems*, 2024.
- [26] S. Li, K. Xue, B. Zhu, and et al., "Falcon: A fourier transform based approach for fast and secure convolutional neural network predictions," in *Proceedings of the IEEE/CVF Conference on Computer Vision and Pattern Recognition*, 2020, pp. 8705–8714.
- [27] Vercellis C. Jalayer M., Orsenigo C., "Fault detection and diagnosis for rotating machinery: A model based on convolutional lstm, fast fourier and continuous wavelet transforms," *Computers in Industry*, vol. 125, pp. 103378, 2021.
- [28] W. Yu and Z. Qin, "Graph convolutional network for recommendation with low-pass collaborative filters," in *International Conference on Machine Learning*. PMLR, 2020, pp. 10936–10945.
- [29] Y. Fang, Z. Wang, L. Zhang, and et al, "Spiking wavelet transformer," in *European Conference on Computer Vision*. Springer, 2025, pp. 19–37.
- [30] A. Shahroudy, J. Liu, T.-T. Ng, and et al, "Ntu rgb+ d: A large scale dataset for 3d human activity analysis," in *Proceedings of the IEEE*

conference on computer vision and pattern recognition, 2016, pp. 1010–1019.

- [31] J. Liu, A. Shahroudy, M. Perez, and et al, “Ntu rgb+ d 120: A large-scale benchmark for 3d human activity understanding,” *IEEE transactions on pattern analysis and machine intelligence*, vol. 42, no. 10, pp. 2684–2701, 2019.
- [32] J. Wang, X. Nie, Y. Xia, and et al, “Cross-view action modeling, learning and recognition,” in *Proceedings of the IEEE conference on computer vision and pattern recognition*, 2014, pp. 2649–2656.
- [33] Wang L. Du Y., Wang W., “Hierarchical recurrent neural network for skeleton based action recognition,” in *Proceedings of the IEEE conference on computer vision and pattern recognition*, 2015, pp. 1110–1118.
- [34] J. Liu, A. Shahroudy, D. Xu, and G. Wang, “Spatio-temporal lstm with trust gates for 3d human action recognition,” in *Computer Vision–ECCV 2016: 14th European Conference, Amsterdam, The Netherlands, October 11–14, 2016, Proceedings, Part III* 14. Springer, 2016, pp. 816–833.
- [35] Z. Liu, H. Zhang, Z. Chen, and et al, “Disentangling and unifying graph convolutions for skeleton-based action recognition,” in *Proceedings of the IEEE/CVF conference on computer vision and pattern recognition*, 2020, pp. 143–152.

APPENDIX

In the appendix, we first provide the supplemental detail description of Legendre Polynomial-Based Filters and pseudocode of the proposed methods, followed by a detailed introduction to the dataset. Then, we describe the hyperparameter settings and training details.

A. Legendre Polynomial-Based Filters

Legendre polynomials $P_k(x)$, defined over the interval $[-1, 1]$, provide a robust orthogonal basis for constructing frequency-domain filters aimed at decomposing spike-like features in temporal signals. Their orthogonality condition ensures that different polynomial orders yield mutually independent basis functions. The polynomials are generated recursively using the relation:

$$\begin{aligned} P_0(x) &= 1, \quad P_1(x) = x, \\ (k+1)P_{k+1}(x) &= (2k+1)xP_k(x) - kP_{k-1}(x). \end{aligned} \quad (22)$$

Their orthogonality condition, as:

$$\int_{-1}^1 P_m(x)P_n(x) dx = \frac{2}{2n+1} \delta_{mn} \quad (23)$$

This property is particularly advantageous for designing a set of filters that can isolate specific frequency components with minimal interference.

To apply these polynomials to time-domain signals sampled over $[0, T]$, we first normalize the time index:

$$u = \frac{t}{T}, \quad u \in [0, 1]. \quad (24)$$

We then map $[0, 1]$ to $[-1, 1]$:

$$x = 2u - 1. \quad (25)$$

This transformation aligns the original time domain with the canonical domain of the Legendre polynomials, ensuring straightforward evaluation of $P_k(x)$ at the corresponding sampling points.

Within this framework, low-frequency (“low-pass”) filters are derived from lower-order Legendre polynomials, which vary slowly across $[-1, 1]$. To ensure proper normalization, each polynomial is scaled by $\sqrt{2k+1}$. Introducing a half-period shift $\Delta = 0.5$ in the normalized time domain allows us to construct two distinct low-pass filters by evaluating the polynomials at slightly different points. Specifically, the low-pass filters are defined as:

$$\Lambda_0[k, t] = \sqrt{2k+1} P_k(2u - 1), \quad (26)$$

$$\Lambda_1[k, t] = \sqrt{2k+1} P_k(2(u + 0.5) - 1) = \sqrt{2k+1} P_k(2u). \quad (27)$$

Here, $\Lambda_0[k, t]$ and $\Lambda_1[k, t]$ share the same polynomial family but are evaluated at $2u - 1$ and $2u$, respectively, introducing a phase-like shift that distinguishes the two filters in their temporal and spectral responses.

For high-frequency (“high-pass”) filters, the ideal construction involves deriving them from multi-resolution analysis

(MRA) conditions to ensure orthogonality and perfect reconstruction. Nonetheless, a representative scheme, consistent with the normalization above, is given by:

$$\Gamma_0[k, t] = \sqrt{2} \Lambda_0[k, t], \quad (28)$$

$$\Gamma_1[k, t] = \sqrt{2} \Lambda_1[k, t]. \quad (29)$$

Taken together, these four filters ($\Lambda_0, \Lambda_1, \Gamma_0, \Gamma_1$) can decompose the signal into distinct frequency bands, enabling a nuanced analysis of spike-like features. By carefully mapping temporal samples into the Legendre polynomial domain, employing a normalized and shifted set of low-pass filters, and incorporating a high-pass counterpart, this approach provides a stable, orthogonal, and frequency-selective analytical framework. This framework facilitates effective characterization, improved interpretability, and subsequent analyses of time-varying signals in a multi-resolution context.

B. Algorithm

This section presents the essential pseudocode and detail description underpinning the computational framework discussed in this work.

1) *Spiking Neuron Dynamics Simulation*: The Spiking Neuron Dynamics describes the core mechanisms governing the temporal dynamics of spiking neurons within the network, outlined in Algorithm 1.

Algorithm 1 Spiking Neuron Dynamics Simulation

```

1: Input:  $G \in \mathbb{R}^{T \times D \times V}$ 
2: Parameters:  $\tau, V_{\text{rest}}, R, V_{\text{th}}$ 
3: Output:  $G_o \in \mathbb{R}^{T \times C \times V}$ 
4: Initialize  $V(t)$  and  $G_o$ 
5: for  $t = 0$  to  $T - 1$  do
6:    $G_i(t) \leftarrow G[t, :, :]$ 
7:    $\tau \frac{dV(t)}{dt} \leftarrow -(V(t) - V_{\text{rest}}) + R \cdot G_i(t)$ 
8:   if  $V(t) \geq V_{\text{th}}$  then
9:      $G_o[t, :, :] \leftarrow 1$ 
10:     $V(t) \leftarrow V_{\text{rest}}$  {Reset voltage after spike}
11:   else
12:      $G_o[t, :, :] \leftarrow 0$ 
13:   end if
14: end for
15: return  $G_o \in \mathbb{R}^{T \times D \times V}$ 

```

The input, $G \in \mathbb{R}^{T \times D \times V}$, represents the temporal sequence of feature maps for T time steps, where D and V denote the feature dimension and the number of vertices (e.g., joints in skeleton data), respectively. The algorithm computes the output $G_o \in \mathbb{R}^{T \times C \times V}$, which represents the spike emissions over time, with C corresponding to the output channel dimension.

At each time step t , the membrane potential $V(t)$ is updated based on the input current $G_i(t)$ and the parameters governing spiking neuron dynamics, including the membrane time constant τ , the resting potential V_{rest} , the resistance R ,

and the firing threshold V_{th} . Specifically, the potential evolves according to the equation:

$$\tau \frac{dV(t)}{dt} = -(V(t) - V_{\text{rest}}) + R \cdot G_i(t), \quad (30)$$

where $G_i(t) = G[t, :, :]$ is the input tensor for time step t . If the membrane potential $V(t)$ exceeds the threshold V_{th} , a spike is emitted ($G_o[t, :, :] = 1$), and the potential is reset to V_{rest} . Otherwise, no spike is generated ($G_o[t, :, :] = 0$).

This mechanism enables the simulation of spike-based information transmission, where G_o captures the spiking behavior at each time step. The tensor G_o has the same temporal and spatial resolution as the input but reflects the binary spike activations, effectively encoding temporal dynamics into discrete spike events.

The iterative process ensures that spiking neurons dynamically respond to varying inputs while adhering to biologically inspired principles. Subsequent layers of spiking neurons follow similar dynamics, allowing the network to propagate spike-based representations through deeper processing stages.

2) *Iterative Decomposition*: The Iterative Decomposition algorithm describes the process of decomposing spike-form features into their frequency domain representations. This hierarchical decomposition enables the separation of temporal dynamics into high-frequency detail coefficients and low-frequency scaling coefficients, which are critical for efficient feature extraction and multi-resolution analysis in SNNs.

Algorithm 2 Iterative Decomposition

```

1:  $X_0 \leftarrow X_{\text{extended}}$ 
2: for  $j = 0$  to  $J - 1$  do
3:    $X_{\text{even}}^{(j)} \leftarrow X_j[:, 2, :, :]$ 
4:    $X_{\text{odd}}^{(j)} \leftarrow X_j[1 :: 2, :, :]$ 
5:    $D_j \leftarrow \Gamma_0 \cdot X_{\text{even}}^{(j)} + \Gamma_1 \cdot X_{\text{odd}}^{(j)}$ 
6:    $S_j \leftarrow \Lambda_0 \cdot X_{\text{even}}^{(j)} + \Lambda_1 \cdot X_{\text{odd}}^{(j)}$ 
7:    $X_{j+1} \leftarrow S_j$ 
8: end for
9:  $S_J \leftarrow X_J$ 
10: return  $\{D_j\}_{j=0}^{J-1}$  and  $\{S_j\}_{j=0}^J$ 

```

The iterative decomposition process begins with the extended spike-form feature tensor X_{extended} , which serves as the initial input. The tensor is initialized as X_0 , providing the starting representation for decomposition across J levels.

At each decomposition level j , the input tensor X_j is divided along its temporal dimension into even and odd indexed components, denoted as $X_{\text{even}}^{(j)}$ and $X_{\text{odd}}^{(j)}$, respectively. These components are independently processed to compute the detail coefficients D_j and scaling coefficients S_j as follows:

$$D_j = \Gamma_0 \cdot X_{\text{even}}^{(j)} + \Gamma_1 \cdot X_{\text{odd}}^{(j)}, \quad (31)$$

$$S_j = \Lambda_0 \cdot X_{\text{even}}^{(j)} + \Lambda_1 \cdot X_{\text{odd}}^{(j)}. \quad (32)$$

where, Γ_0, Γ_1 are high-pass filter matrices used to extract the detail coefficients D_j , which capture high-frequency temporal

variations. Conversely, Λ_0, Λ_1 are low-pass filter matrices that compute the scaling coefficients S_j , preserving the low-frequency temporal information.

After computing D_j , the scaling coefficients S_j are propagated to the next level by setting $X_{j+1} = S_j$. This iterative decomposition continues across all J levels, refining the temporal representation at each step. Upon completing the J -th level, the final scaling coefficients S_J are obtained. The process outputs the set of detail coefficients $\{D_j\}_{j=0}^{J-1}$ and scaling coefficients $\{S_j\}_{j=0}^J$, providing a hierarchical representation of the temporal dynamics.

Upon completion, the algorithm outputs a set of detail coefficients $\{D_j\}_{j=0}^{J-1}$ and the final scaling coefficients S_J , collectively encapsulating the hierarchical temporal structure of the input. The complete iterative decomposition process is outlined in Algorithm 2, providing a systematic and computationally efficient method for processing spike-form feature.

C. Datasets

1) *NTU-RGB+D*: NTU-RGB+D [30] is a comprehensive dataset widely used in the field of skeleton-based action recognition. It contains 60 action classes and 56,000 video clips, making it a robust benchmark for evaluating action recognition models. The dataset provides detailed 3D skeleton data, RGB frames, depth maps, and infrared sequences, covering a diverse range of daily activities such as eating, walking, and interacting with objects. The skeleton data consists of 25 joints per subject, captured using the Microsoft Kinect v2 sensor, which allows for precise modeling of human movement. This dataset is particularly valuable for researchers because it includes a variety of subjects performing actions from multiple viewpoints, offering a rich source of information to develop and test models capable of understanding complex human behaviors.

2) *NTU-RGB+D 120*: NTU-RGB+D 120 [31] is an extended version of the original NTU-RGB+D dataset, expanding the number of action classes from 60 to 120 and increasing the total number of video clips to over 114,000. This extension includes additional action categories that encompass more complex and subtle human interactions, such as "taking a selfie" and "writing on a board." With 106 distinct subjects and more diverse camera angles, NTU-RGB+D 120 offers a more challenging and comprehensive benchmark for evaluating the scalability and generalization capabilities of action recognition models. The dataset retains the detailed skeleton tracking of its predecessor, providing 25 joints per person and ensuring that the data remains highly informative for developing models that require an in-depth understanding of spatial-temporal dynamics in human actions. As one of the largest skeleton-based action recognition datasets available, NTU-RGB+D 120 is instrumental in pushing the boundaries of research in this field.

3) *NW-UCLA*: The NW-UCLA dataset [32] is a smaller but uniquely challenging dataset consisting of 10 action classes and 1,494 video clips. It is specifically designed to test the robustness of action recognition models against viewpoint

variations. The dataset features actions like jumping, waving, and running, captured from multiple viewpoints using three Kinect cameras placed at different angles. Each action is performed by 10 subjects, offering diverse skeleton data with 20 joints per person. This setup mimics real-world scenarios where actions are observed from different perspectives, making it a critical dataset for evaluating how well models can maintain performance when faced with varying observational conditions. The NW-UCLA dataset is ideal for researchers aiming to enhance the adaptability and resilience of their models to changes in camera viewpoints, which is essential for applications in surveillance, human-computer interaction, and robotics.

D. Model Implementation and Configuration

The models used for conducting experiments are implemented using PyTorch¹, a classical deep learning framework known for its flexibility and efficiency, and SpikingJelly², a specialized library for spiking neural network research. Our implementation leverages the powerful features of these tools to effectively model and simulate the complex dynamics of spiking neural networks. The training process is conducted on four NVIDIA V100 GPUs, which provide the necessary computational power and memory to handle the large datasets and intricate computations involved in our experiments. This setup ensures that our models are trained efficiently, allowing us to explore the full potential of our approach in a scalable and robust manner.

TABLE IV
THE PARAMETER SETTINGS OF THE BACKBONE

Level of Layers	Channel Size	
	Input	Output
1	3	64
2	64	64
3	64	128
4	128	256

In this section, we also give the specific hyperparameters of the model and training settings in all experiments. Table IV. presents the parameter settings of the backbone network, detailing the input and output channel sizes across different layers to illustrate the model's architectural configuration.

The various hyperparameter settings used in our experiments are also shown in the TableV.

E. Power Consumption

We assume that multiply-and-accumulate (MAC) and accumulate (AC) operations are implemented on the 45 nm technology node with $E_{MAC} = 4.6$ pJ and $E_{AC} = 0.9$ pJ. The FLOPs for Signal-SGN and all reproduced models are calculated using FVCore³, providing accurate estimates for each model component. These FLOPs are then combined with the firing rate and spike time steps to compute SOPs as:

¹<https://github.com/rwightman/pytorch-image-models>

²<https://github.com/fangwei123456/spikingjelly>

³<https://github.com/facebookresearch/fvcore>

TABLE V
HYPER-PARAMETER TRAINING SETTINGS OF SIGNAL-SGN.

Parameter	NTU-RGB+D 60	NTU-RGB+D 120	NW-UCLA
Learning Rate	0.1/0.1	0.1/0.1	0.1/0.1
Decay rate	0.1/0.1	0.1/0.1	0.1/0.1
Batch Size	64	64	128
Training Epochs	90	90	90
Step	50	50	50
Dropout Rate	0.3	0.3	0.3
Weight Decay	1e-4	1e-4	1e-4
ω	0.03	0.03	0.03
Optimizer	SGD	SGD	SGD

$$\text{SOPs}(l) = fr \times T \times \text{FLOPs}(l), \quad (33)$$

where fr is firing rate, T is the spike time steps, $\text{FLOPs}(l)$ refers to the floating-point operations of l , defined as the number of MAC operations performed in l block or layer, and SOPs are the number of spike-based AC operations.

The model's theoretical energy consumption is described as:

$$E_{\text{Signal-SGN}} = E_{\text{EAC}} \times \text{FL}_{\text{SNN Conv}}^1 + \\ E_{\text{AC}} \times \left[\left(\sum_{n=2}^N \text{SOP}_{\text{SNN Conv}}^n + \sum_{m=1}^M \text{SOP}_{\text{SNN FC}}^m \right) + \sum_{l=1}^L \text{SOP}_{\text{SNN SSA}}^l + \sum_{f=1}^F \text{SOP}_{\text{SNN FFT}}^f \right] + \text{SOP}_{\text{SNN MWTF}} \quad (34)$$

where $\text{FL}_{\text{SNN Conv}}^1$ is the first layer to encode skeleton into spike-form. Then the SOPs of N SNN Conv layers, M SNN Fully Connected Layer (FC), L SSA, F SSA and MWTF are added together and multiplied by E_{AC} . The theoretical energy consumption for ANN and SNN models is calculated as follows:

For ANNs, the energy consumption of a block b is given by:

$$\text{Power}(b) = 4.6 \text{ pJ} \times \text{FLOPs}(b). \quad (35)$$

For SNNs, the energy consumption of a block b is given by:

$$\text{Power}(b) = 0.9 \text{ pJ} \times \text{SOPs}(b). \quad (36)$$

F. More detail of Ablation Studies

In this section, we provide additional details regarding the ablation studies conducted in our research. These experiments are designed to investigate the contribution of various components within our framework and to demonstrate the effectiveness of specific design choices. By systematically removing or altering key elements, we aim to provide a deeper understanding of their impact on the overall performance.

a) *3D coordinate normalization*: 3D skeleton data often spans multiple quadrants and includes negative values, as shown in Figure 2, creating challenges for SNNs, which are inherently designed for non-negative numerical inputs. Negative coordinates lead to significant information loss and degrade model performance. To address this limitation, 3D

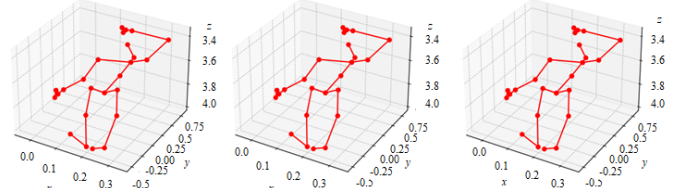


Fig. 2. 3D Skeleton Visualization

TABLE VI
IMPACT OF 3D COORDINATE NORMALIZATION ON ACCURACY

3D Coord. Norm.	1D-SGC	FSC	MWTF	Acc (%)
-	✓	-	-	69.7
-	✓	✓	-	77.0
-	✓	✓	✓	79.3
✓	✓	-	-	70.5
✓	✓	✓	-	78.3
✓	✓	✓	✓	80.5

coordinate normalization is applied to map skeleton data into a fixed and bounded range, ensuring numerical consistency and preserving essential information. Normalization facilitates stable data propagation through the network by mitigating discrepancies arising from varying magnitudes and signs.

The analysis focuses primarily on accuracy as the evaluation metric, as changes in parameters and FLOPs introduced by normalization are minimal. By isolating the impact of 3D coordinate normalization on accuracy, the study demonstrates that normalization significantly enhances model performance without introducing substantial computational overhead. Controlled experiments under various module configurations reveal consistent accuracy improvements, underscoring this approach's effectiveness in processing complex skeleton data. Detailed results presented in the accompanying table highlight the practical benefits of normalization in achieving higher accuracy with negligible computational trade-offs.

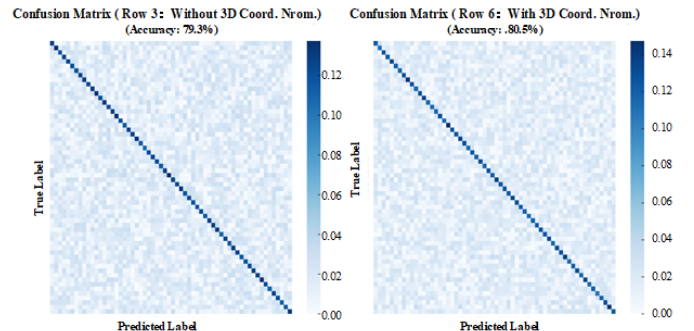


Fig. 3. Comparison of confusion matrices for full-module integration setup with and without 3D coordinate normalization

The results in Table 3 demonstrate the significant role of 3D coordinate normalization in improving accuracy across all module configurations. For the baseline configuration (1D-SGC only), normalization increases accuracy by 0.8%, while

TABLE VII
COMPARISON OF EXPERIMENTAL RESULTS UNDER DIFFERENT MWTF SETTINGS (k AND J)

MWTF	k	J	Param. (M)	FLOPs/SOPs (G)	Acc (%)
-	-	-	1.65	1.60/0.312	78.3
✓	4	1	1.68	1.61/0.313	78.9
✓	8	1	1.73	1.62/0.314	79.8
✓	8	2	1.74	1.62/0.315	80.3
✓	8	3	1.74	1.62/0.317	80.5
✓	16	3	1.83	1.64/0.320	80.5

in more complex setups with FSC and MWTF modules, the improvements reach 1.3% and 1.2%, respectively. This indicates that normalization effectively stabilizes the input data by addressing inconsistencies in coordinate ranges, enabling the model to better utilize its capacity. Importantly, the improvements in accuracy are achieved without notable changes in parameters or computational cost, highlighting normalization as a practical and efficient enhancement for processing 3D skeleton data. To further analyze the impact of 3D coordinate normalization, we selected the full-module integration setup (MWTF enabled) from the third and sixth rows of Table VI and visualized the corresponding confusion matrices.

b) Different Settings for MWTF: To investigate the impact of different configurations of k (frequency resolution) and J (decomposition levels) on the performance of the MWTF module within **Signal-SGN**, we conduct a series of controlled experiments. The overall architecture of Signal-SGN is kept unchanged, ensuring that any observed variations in performance can be attributed solely to changes in the MWTF parameters. By systematically adjusting k and J , we aim to analyze how the trade-off between frequency granularity and decomposition depth affects the network's ability to extract and fuse temporal features effectively.

The experimental results in Table VII highlight the impact of varying k (frequency resolution) and J (decomposition levels) on the performance of the MWTF module within Signal-SGN. With the overall architecture unchanged, the table isolates the influence of MWTF parameters, providing insight into their effects on accuracy, computational complexity, and parameter efficiency.

When MWTF is disabled, the model achieves a baseline accuracy of 78.3% with a parameter count of 1.65M and computational costs of 1.60/0.312 G (FLOPs/SOPs). Enabling MWTF with different k and J configurations demonstrates significant improvements. As k increases from 4 to 8, accuracy improves substantially, with the model achieving 79.8% ($k = 8, J = 1$). Further increasing k to 16 yields diminishing returns, with accuracy peaking at 80.5% for $k = 16, J = 3$.

Similarly, increasing J allows for deeper decomposition of temporal features, which enhances performance up to a point. For example, with $k = 8$, accuracy improves from 79.8% ($J = 1$) to **80.7%** ($J = 3$). This configuration achieves the best accuracy while maintaining a parameter count of 1.74M and computational cost of 1.62/0.317 G. Further increasing k

to 16 ($J = 3$) slightly reduces accuracy to 80.5%, indicating that excessively high frequency resolution or decomposition depth might lead to redundant features or overfitting.

Overall, the results demonstrate that the MWTF module significantly enhances the performance of Signal-SGN when configured optimally. The configuration $k = 8, J = 3$ emerges as the most effective setting, balancing frequency granularity, decomposition depth, and computational efficiency, and achieving the best accuracy of 80.7%. This underscores the importance of selecting appropriate MWTF parameters to maximize feature extraction and model performance.